


OPEN ACCESS
EDITED BY

 Joana Mesquita—Guimarães,
University of Aveiro, Portugal

REVIEWED BY

 Pavlo Maruschak,
Ternopil Ivan Pului National Technical
University, Ukraine
Chen Ji,
Chongqing University, China

***CORRESPONDENCE**

 Shuyang Liu,
✉ 50180425@qq.com
Zhihong Han,
✉ 002700@jcu.edu.cn

RECEIVED 07 November 2025

REVISED 24 February 2026

ACCEPTED 25 February 2026

PUBLISHED 12 March 2026

CITATION

 Han Z, Wang Y, Liu S and Hu J (2026)
Experimental study on the influence of
gradient structure design on the
thermal response behavior of
composite materials.
Front. Mater. 13:1741731.
doi: 10.3389/fmats.2026.1741731

COPYRIGHT

 © 2026 Han, Wang, Liu and Hu. This is
an open-access article distributed
under the terms of the [Creative
Commons Attribution License \(CC BY\)](#).
The use, distribution or reproduction in
other forums is permitted, provided the
original author(s) and the copyright
owner(s) are credited and that the
original publication in this journal is
cited, in accordance with accepted
academic practice. No use, distribution
or reproduction is permitted which
does not comply with these terms.

Experimental study on the influence of gradient structure design on the thermal response behavior of composite materials

 Zhihong Han^{1*}, Yaoqian Wang², Shuyang Liu^{3*} and Junjie Hu²
¹College of Artificial Intelligence, Putian University, Putian, Fujian, China, ²School of Mechanical and Electronic Engineering, Jingdezhen Ceramic University, Jingdezhen, China, ³College of Intelligent Manufacturing, Putian University, Putian, Fujian, China

This study investigates how gradient layer thickness affects the thermal response of CuSn10/316L stainless steel composites fabricated by selective laser melting (SLM). Three gradient architectures with varying layer thicknesses were designed and analyzed through both simulation and experiment. Simulations predicted that increasing interfacial layers would enhance thermal barrier performance. However, experimental results showed the opposite trend: samples with thinner layers and lower porosity (10.03%) exhibited poorer thermal barrier properties, while those with thicker layers and higher porosity (15.42%) performed best. This discrepancy reveals that porosity—governed by layer thickness—is the dominant factor controlling thermal behavior, outweighing the effect of interfacial density. Thicker layers promote heat accumulation and gas entrapment, increasing porosity and thermal resistance. The findings establish a clear pathway from gradient layer thickness to porosity evolution to thermal response, providing practical guidance for designing functionally graded materials with tailored thermal barrier performance.

KEYWORDS

composite material, gradient structure, porosity, selective laser melting, thermal barrier performance, thermal response

1 Introduction

Composite materials are widely valued in fields such as aerospace, energy, and electronic devices (Balakrishnan et al., 2016; Yen and Liou, 2019) due to their lightweight nature, high strength, corrosion resistance, and excellent thermal performance. By combining the advantages of multiple constituents, these materials meet stringent structural and functional requirements, thereby enhancing the overall performance of complex systems. However, traditional manufacturing techniques for composites (Pandey et al., 2024) face significant limitations in terms of performance and shape design, which restricts their application potential. Processes such as chemical vapor deposition (Cai et al., 2018; Choy, 2003), powder metallurgy (Liu et al., 1994), and centrifugal casting (El-Galy et al., 2017) encounter challenges in ensuring material compositional uniformity, microstructural control, and multifunctional integration (Hasanov et al., 2021; Cadman et al., 2013; Guo et al., 2023; Narayana and Burela, 2018). In particular, issues such as gradient transitions (Markworth et al., 1995; Tonyali et al., 2024a) and interfacial bonding strength (Tan et al., 2021; Zhang et al., 2019) often exceed the capabilities of conventional methods. With advances in science and technology, the need for microscale optimization of composites has become increasingly prominent, necessitating breakthroughs beyond traditional

manufacturing approaches to enable new solutions for multifunctional material design (Tonyali et al., 2024b; Thomas and Qidwai, 2004; Yuan et al., 2021; Ferreira et al., 2016).

To address these challenges, additive manufacturing (AM) technologies (Tofail et al., 2018; Li et al., 2021; Attar et al., 2018; Shi and Wang, 2020), particularly Selective Laser Melting (SLM) (Yap et al., 2015), have attracted considerable research interest due to their unique advantages in fabricating complex materials. SLM enables precise control over microstructures through layer-by-layer selective melting of metal powders (Najmon et al., 2019; Liu et al., 2022), fulfilling requirements for complex geometries and functional integration (Markandan et al., 2020). This technology offers distinct benefits in high-resolution fabrication and multi-material composite systems. By accurately controlling laser energy density, the SLM process not only reduces material porosity (Du Plessis et al., 2020; AlMangour et al., 2017) but also enhances interfacial bonding quality, thereby significantly expanding its potential applications in aerospace, thermal management (Sidhu et al., 2016), and energy-related fields.

As an innovative design strategy, gradient structures (Markworth et al., 1995) can markedly improve the overall performance of composites by tailoring compositional transitions and structural arrangements between materials. Gradient designs allow optimization of thermal conductivity distribution in thermal management systems (Davis and Artz, 1995) and help mitigate interfacial thermal stress resulting from differences in thermal expansion coefficients (Pang et al., 2022). For example, CuSn10–316L stainless steel composites (Raghavendra et al., 2023) have gained research attention owing to their distinctive thermal and mechanical properties. CuSn10 exhibits high thermal conductivity (up to 400 W/(m·K)), making it suitable for heat exchangers and radiators, whereas 316L stainless steel offers moderate thermal conductivity (15–30 W/(m·K)), high mechanical strength, and corrosion resistance, rendering it applicable in complex stress environments. Supported by SLM technology, these two materials can be integrated via gradient structure design to effectively optimize interfacial characteristics, achieving synergistic enhancements in both mechanical and thermal performance (Sathish et al., 2021).

Despite the theoretical and practical potential of gradient design, its implementation during SLM fabrication presents several challenges. On one hand, gradient structures require smooth compositional transitions at the interface to avoid cracks and porosity caused by inadequate bonding. On the other hand, the relationship between porosity and thermal conductivity (Dai and Gu, 2014) remains insufficiently understood. Previous studies indicate that optimizing gradient layer thickness can effectively reduce porosity, increase material density, and improve interfacial bonding strength (Yang et al., 2020; Mao et al., 2023). Addressing these challenges requires a combined experimental and theoretical approach to systematically analyze the effects of gradient designs on microstructure and functional performance. Advances in SLM parameter optimization directly inform gradient design strategies. Although transition layers help mitigate cracking, their thermal regulation mechanisms are not fully quantified. For instance, Darabi's phase-field model (Darabi et al., 2023) (with < 5% error in critical temperature prediction) does not account for electromagnetic–fluid interactions, which are crucial to SLM thermal dynamics. Furthermore, the influence of scanning speed on

thermal cycling frequency a key factor for gradient layer integrity lacks experimental quantification, and real-time monitoring of interfacial thermal resistance remains unresolved.

This knowledge gap is particularly critical for dissimilar metal composites, where thermomechanical synergy governs performance. To address this, the present study investigates how gradient layer design controls thermal response in SLM-fabricated CuSn10/316L composites. Computational modeling was used to systematically evaluate the sensitivity of heat transfer to variations in gradient layer thickness. Complementary single-factor experiments produced SLM specimens with controlled thickness gradients for thermal characterization. Simulations assuming porosity-free interfaces predicted improved thermal barrier performance with increased interfacial layers. Crucially, experimental results revealed that porosity-dominated thermal impedance outweighed the simulated benefits of additional interfaces, leading to anomalous thermal underperformance in multi-interface specimens. Therefore, quantifying porosity formation in gradient designs emerges as a critical pathway toward predictable thermal management. This work establishes gradient layer architecture as a primary means of controlling thermal response in SLM composites and provides actionable design principles for thermally-graded materials focused on barrier performance.

2 Materials and methods

2.1 Multi-material SLM equipment and materials

The experiments were conducted using the LASERADD Dimetal-150 multi-material selective laser melting (SLM) system, as shown in Figure 1A. The main equipment parameters are listed in Table 1. The Dimetal-150 is equipped with a 500 W ytterbium-doped fiber laser and a high-precision galvanometric scanning system, capable of a scanning speed up to 8 m s⁻¹ to meet the efficiency demands for fabricating complex structures.

As shown in Figure 1B, the equipment features two powder feeding systems: powder cylinder 1 supplies powder from bottom to top, whereas powder cylinder 2 delivers powder from top to bottom. A recoater moves inside the build chamber to spread powder from the feed bars. Prior to laser sintering, the chamber is purged with argon to reduce the oxygen content below 0.01% (1,000 ppm), thereby minimizing metal oxidation and limiting impurities from combustion or vaporization.

The materials used in this study were 316L stainless steel powder and CuSn10 alloy powder. Both powders were produced by high-purity argon gas atomization and supplied by Guangzhou LASERADD Additive Manufacturing Co., Ltd. The particle size distribution ranged from 15 to 53 μm for both materials. Their chemical compositions are listed in Table 2.

2.2 Process parameters

The samples were fabricated as square layers measuring 15 mm × 15 mm, with a constant layer thickness of 0.03 mm and a total of 110 layers. The thickness of the gradient structural layers was designed to vary linearly, producing three distinct sample

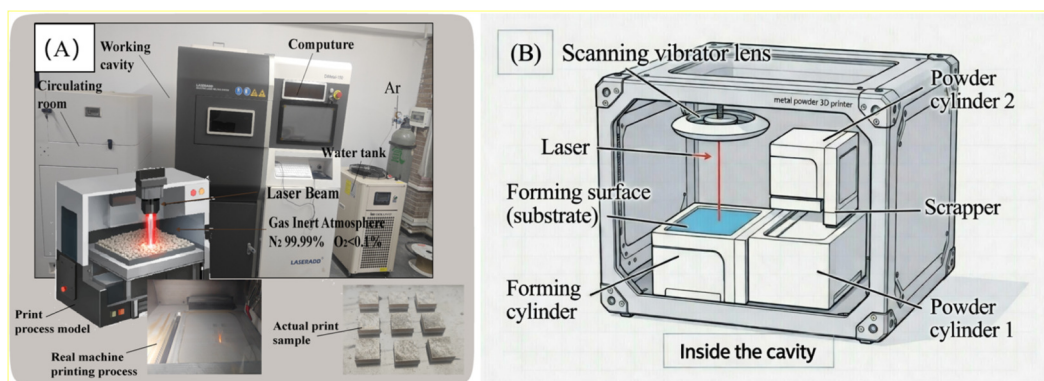


FIGURE 1 SLM equipment and its working principle. (A) Photograph of the experimental setup; (B) Schematic of the working principle.

TABLE 1 Dimetal-150 SLM equipment parameters.

Item	Parameter/Specification
Laser	IR ytterbium-doped fiber laser, 500 W
Scanning system	High-precision galvanometric scanner
Scanning speed	Up to 8 m s ⁻¹
Build volume	170 mm × 170 mm × 200 mm
Layer thickness	20–200 μm
Power supply	220 V, 50 Hz, 5 kW
Operating temperature	15 °C–30 °C

configurations. The variation in gradient layer thickness is illustrated in Figure 2A, where “S” denotes stainless steel and “C” denotes CuSn10. The horizontal axis represents the layer number, and the vertical axis (from bottom to top) indicates the material sequence along the build direction—corresponding to the physical bottom-to-top order of the printed sample. It should be noted that the gradient architecture in this study was achieved through programmed modulation of layer thickness and stacking sequence, rather than the continuous powder blending commonly used in classical functionally graded materials (FGMs). In this design strategy, the gradient is realized by deliberately alternating the deposited materials in an S–C–S–C ... sequence. In Figure 2A, the horizontal axis reflects the programmed variation in layer thickness, while the vertical axis shows the corresponding material alternation along the build direction. This layer-by-layer distribution aligns with the deposition pattern and material-color transitions observed in the actual printed samples shown in Figure 2B.

For the Dimetal-150 equipment used in this study, orthogonal experimental studies (Yan et al., 2019) were first performed on single-material process parameters to achieve optimal relative density. The resulting optimized parameters are summarized in Table 3. To ensure process consistency and systematic fabrication, bidirectional scanning (Marattukalam et al., 2020) without regional partitioning was applied across the entire single-layer rectangular area (15 mm × 15 mm), as illustrated in Figure 2B.

To improve overall mechanical performance, especially along the Z-axis (build direction), an interlayer cross-scanning strategy (Ullah et al., 2022) was implemented. This approach rotates the scan vectors within each layer and alternates the orthogonal scanning direction between successive layers. The fill angles were systematically alternated between 270° and 315° to enhance microstructural density and material properties. All samples were manufactured using the same set of process parameters, with the only variable being the layer-thickness ratio (i.e., number of layers per material). The specific parameters for fabricating 316L stainless steel and CuSn10 were derived from the single-material optimization results listed in Table 3.

2.3 Microstructural characteristics

To analyze the microstructures of the SLM-fabricated CuSn10-316L stainless steel composites, samples with optimized gradient designs were selected. Cross-sections were prepared using focused ion beam (FIB) milling (Ishitani et al., 1996) to expose the interfacial regions for high-quality microscopic observation. The samples were sequentially ground and polished to achieve a smooth surface, followed by etching with a diluted aqua regia solution (H₂O : HNO₃ : HCl = 6 : 1 : 3) for 12 s (Sathish et al., 2021) to reveal the microstructural features of the metal matrix. After etching, the samples were cleaned with alcohol, dried, and mounted in thermosetting phenolic resin for further analysis.

Scanning electron microscopy (SEM) was employed to examine the cross-sectional microstructures and interfacial regions, as well as to identify micro-defects such as pores and cracks. Based on the constituent elements (Cu, Sn, Fe, Cr, Ni, Mo, and Mn) present in the materials, characteristic X-ray energy values were measured at the interface. The acquired X-ray spectral data (Du Plessis et al., 2020) were processed using quantitative analysis software to generate elemental distribution maps and line scans, thereby revealing compositional transition characteristics and the influence of gradient structures on the interfacial microstructural morphology.

TABLE 2 Chemical compositions of 316L stainless steel and CuSn10 alloy powders (wt. %).

Element	Fe	Cr	Ni	Mo	Mn	Cu	Sn	Other
316L stainless steel	66.28	17.51	12.73	2.56	0.11	—	—	0.89
CuSn10	—	—	—	—	—	89.71	10.23	<0.06

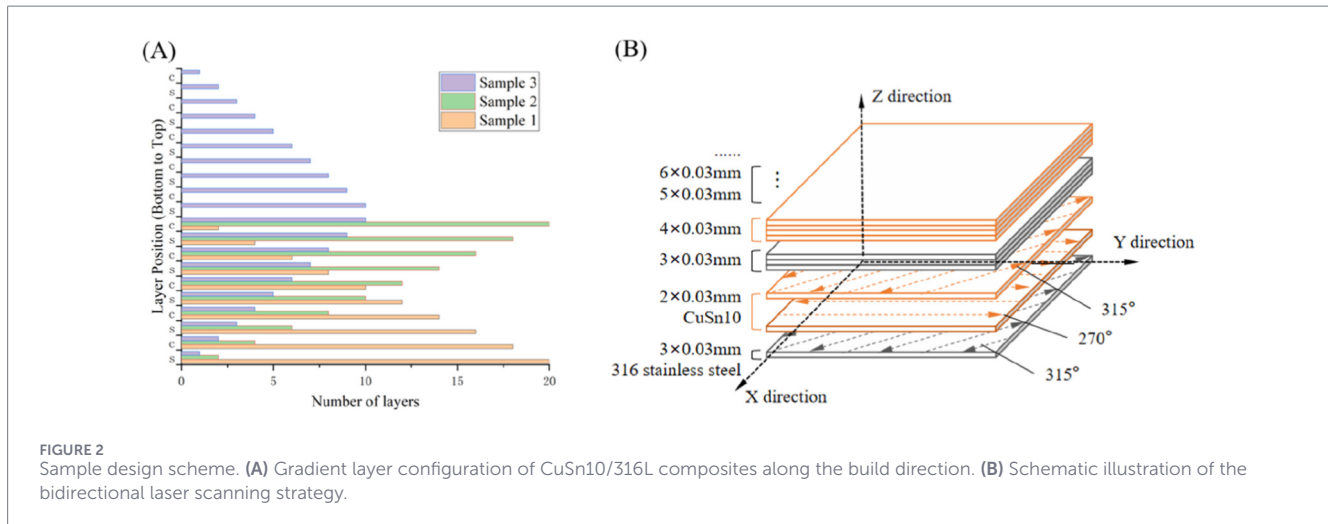


TABLE 3 Optimization results of the process parameters of a single material.

Process parameter	316LStainless steel	CuSn10
Laser power (W)	170	300
Fill spacing (mm)	0.06	0.085
Sweep speed (mm/s)	1,000	700
Print layer thick (mm)	0.03	0.03
Spot diameter (mm)	0.1	0.1

2.4 Thermal conductivity

For the gradient-structured specimens, a thermal conduction simulation model was established for validation. The model assumed 100% relative density to exclude pore-related defects introduced during SLM fabrication, and a uniform thermal contact resistance of $5 \times 10^{-6} \text{ K m}^2 \cdot \text{W}^{-1}$ was applied at each dissimilar material interface. The analysis considered only Fourier heat conduction, neglecting convective and radiative effects, and was based on the 3D transient heat transfer Equation 1 as follows:

$$\rho C_p \frac{\partial T}{\partial t} + \nabla \cdot (-k \nabla T) = Q \tag{1}$$

where ρ is the material density ($\text{kg} \cdot \text{m}^{-3}$), C_p the isobaric specific heat capacity ($\text{J} \cdot \text{kg}^{-1} \cdot \text{K}^{-1}$), $\partial T / \partial t$ the temperature change rate ($\text{K} \cdot \text{s}^{-1}$), and k the thermal conductivity tensor ($\text{W} \cdot \text{m}^{-1} \cdot \text{K}^{-1}$). The boundary conditions imposed a constant temperature of 393.15 K at the

bottom surface, while the top surface was exposed to ambient air under natural convection conditions.

To establish a baseline for comparison, three model configurations with systematically increased interfacial densities were constructed while maintaining identical overall compositional fractions and nominal gradient characteristics. As shown in Figure 3A, these configurations employ an equal and strictly alternating distribution of the two constituent materials, with only the number of uniformly arranged layers being modulated. This controlled design allows the isolation and examination of the intrinsic role of interfacial frequency in governing heat-transfer behavior. Figure 3B further presents five numerical models corresponding to the three experimentally fabricated linear-gradient architectures, supplemented by reference structures of pure copper and pure stainless steel. Under a fixed 1:1 Cu-to-stainless-steel material ratio and assuming a porosity-free domain, these models delineate the attainable heat-transfer responses associated with the three gradient-design strategies detailed in Section 3.3 and realized in the physical specimens. This simulation assumes the material to be fully dense (0% porosity) and is intended to isolate the influence of the gradient structure itself on heat transfer, thereby providing a theoretical benchmark for subsequent experimental analysis. The pores generated during SLM fabrication are expected to significantly affect thermal conductivity, especially as pore accumulation in high-gradient layers may further enhance thermal resistance. These effects will be compared and discussed in Section 3.3 alongside the experimental results.

To comprehensively evaluate the thermal conductivity of the gradient composites (Davis and Artz, 1995; Pang et al., 2022), real-time surface temperature monitoring (Figure 4A) was employed to assess heat transfer along the direction of thermal flux.

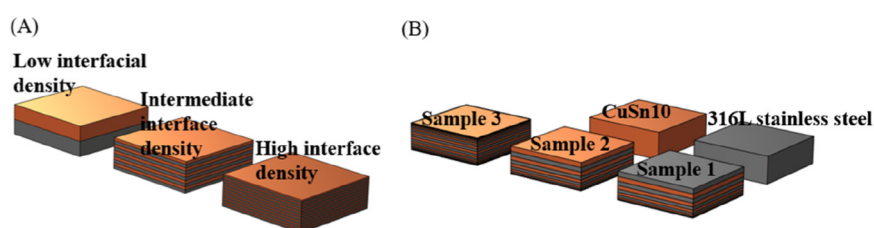


FIGURE 3 Simulation models for thermal analysis. (A) Pre-experimental model with controlled interfacial density. (B) Gradient sample design models used for simulation.

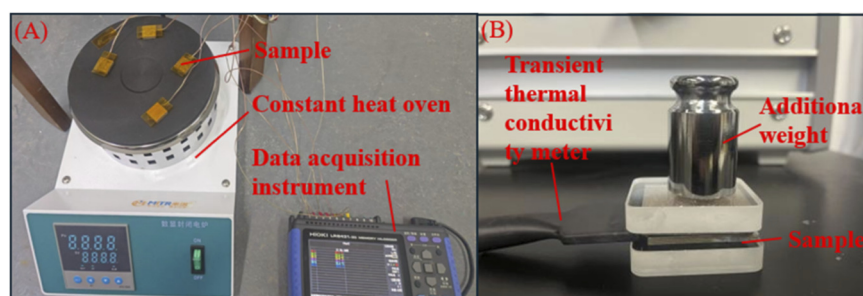


FIGURE 4 Experimental setup for thermal characterization. (A) Surface temperature data acquisition during thermal conduction testing. (B) Transient thermal conductivity measurement setup.

Thermocouples were used to simultaneously record the surface temperatures of three specimens, each in secure contact with an isothermal heating stage. Thermal excitation was applied perpendicular to the gradient-layered architectures. The heating stage was programmed to ramp from ambient temperature (20 °C) to 110 °C, while transient temperature profiles were synchronously acquired at both the specimen surfaces and the substrate. Temperature-time curves corresponding to specific layers were subsequently analyzed to quantify the thermal conduction performance of the samples. For transient hot-wire tests, gradient designs identical to those described above were scaled to dimensions of 30 mm × 40 mm × 3.3 mm. Contact surfaces were polished to a roughness of $R_a < 0.1 \mu\text{m}$ to ensure optimal thermal contact. Specimens were positioned symmetrically above and below the sensor. The experimental setup is shown in Figure 4B.

3 Results and discussion

3.1 Microstructure of the cross-sectional interface

To examine whether compositional saturation or selective sintering occurred during fabrication, metallographic analysis and energy-dispersive spectroscopy (EDS) mapping were performed, as shown in the figures below. These analyses aimed to identify potential compositional enrichment, selective sintering, or

other chemical inhomogeneities resulting from the composite fabrication process.

EDS mapping (Figure 5) revealed clear gradient transitions in elemental distribution across the CuSn10/316L stainless steel interface. The copper (Cu) signal gradually decreased from the CuSn10 region toward the interface, whereas signals from iron (Fe) and chromium (Cr) increased from the stainless steel side toward the interface. No new phases were observed at the interface, nor was obvious segregation or enrichment of elements detected. These results indicate that the SLM process parameters were generally suitable, avoiding elemental migration or electrochemical reactions that could be triggered by excessive heat input or prolonged cooling within the micro-molten pool.

Maximum porosity in the composite was predominantly located at the biphasic interfaces. Notably, the average porosity within individual gradient layers varied only slightly despite increases in layer thickness. This trend is attributed to thermal stresses arising from differences in thermal expansion coefficients at the interface, which can reduce bonding strength.

Copper was primarily concentrated in the CuSn10 region and gradually diminished toward the interface. The Sn signal remained relatively weak in the transition zone, indicating limited interfacial adhesion contribution from Sn. Iron and chromium signals were strongest within the stainless steel region and decreased progressively toward the interface, reflecting sound interfacial bonding after laser melting. Regions of higher porosity at the interface corresponded to areas with weaker Cu and Sn signals,

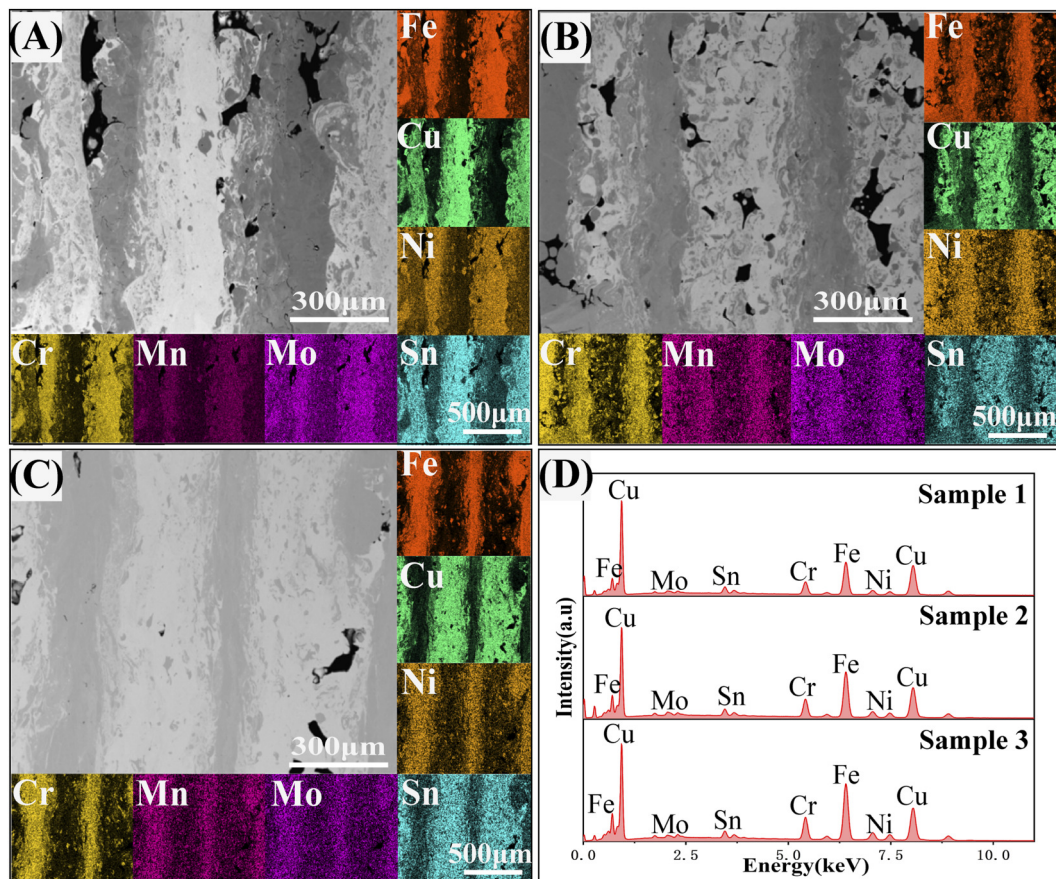


FIGURE 5 Energy dispersive X-ray spectroscopy (EDS) analysis of the interfacial region. (A–C) Elemental distribution maps for samples 1, 2, and 3, respectively; (D) representative EDS spectrum.

suggesting that incomplete melting during bonding contributed to pore formation.

The quantitative EDS results (Table 4) corroborate this observation. Across Samples 1–3, Cu increases from 42.26 to 52.18 wt%, accompanied by a corresponding decrease in Fe (36.14–28.41 wt%) and Cr (9.72–7.74 wt%), consistent with the designed gradient architecture. Minor alloying elements (Mn, Mo, Ni) remain within narrow compositional ranges, and no anomalous enrichment or depletion is observed. The absence of compositional overshoot indicates that neither preferential evaporation nor selective solute accumulation occurred during rapid solidification. These results confirm that compositional evolution is governed primarily by the designed layer sequence rather than by thermally induced segregation. The gradient structure design promoted a smooth compositional transition across the interface, avoiding issues such as selective melting or local solute saturation. Micro cracks and porosity showed a positive correlation with changes in compositional distribution within the interfacial region. EDS mapping confirmed the capability of SLM to achieve uniform melting during the fabrication of gradient composite materials.

The gradient structured stainless steel–CuSn10 bimetallic materials fabricated by SLM are presented in Figures 6A–C for samples 1, 2, and 3, respectively. Cross-sectional microstructures

TABLE 4 EDS quantitative analysis of three representative samples (wt%).

Element	Sample 1	Sample 2	Sample 3
Cr	9.72 ± 0.02	9.16 ± 0.04	7.74 ± 0.04
Mn	0.35 ± 0.02	0.30 ± 0.03	0.30 ± 0.03
Fe	36.14 ± 0.04	33.71 ± 0.07	28.41 ± 0.07
Ni	5.49 ± 0.03	5.21 ± 0.05	4.23 ± 0.05
Cu	42.26 ± 0.05	45.15 ± 0.08	52.18 ± 0.09
Mo	1.55 ± 0.03	1.41 ± 0.05	1.22 ± 0.06
Sn	4.49 ± 0.02	5.06 ± 0.04	5.92 ± 0.05
Total	100.00	100.00	100.00

along the build direction show distinct material layers. The nominal layer thickness was set to 0.03 mm, with blue regions representing stainless steel layers and orange regions representing CuSn10 layers.

As indicated in Figure 6C, the material layers can be categorized into three distinct regions: the 316L stainless steel region, the fusion zone, and the CuSn10 region. For thinner gradient layers,

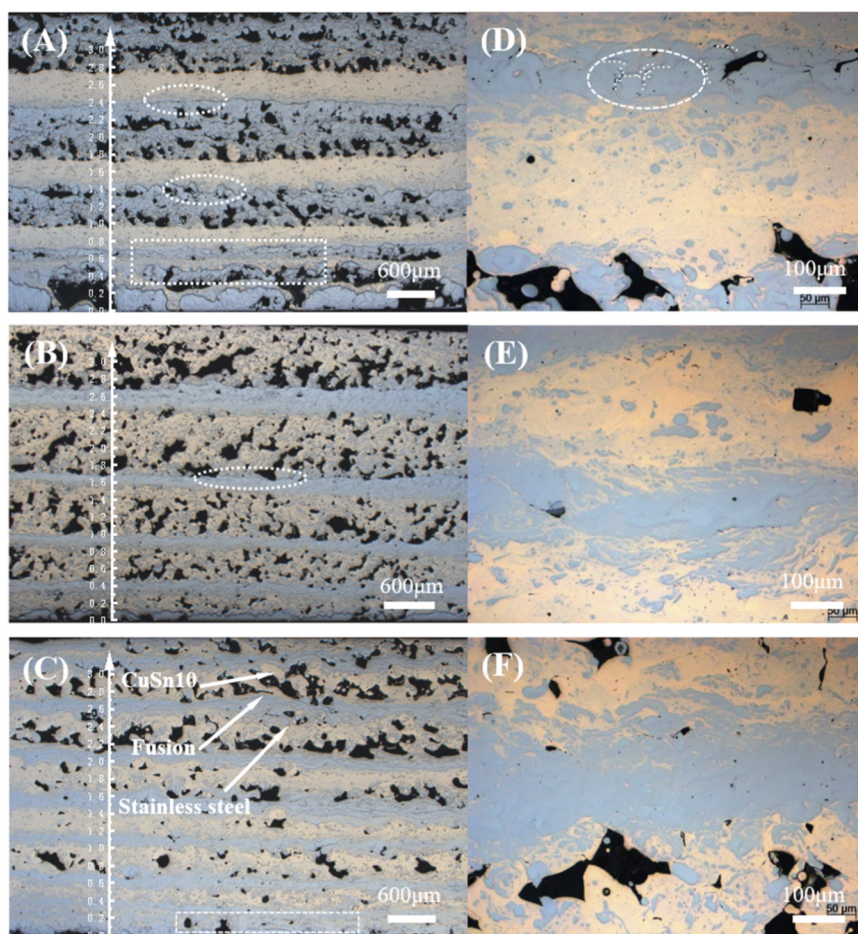


FIGURE 6 Cross-sectional metallographic tissue morphology of each sample: (A) low-magnification morphology; (B) low-magnification morphology; (C) low-magnification morphology; (D) middle-magnification morphology; (E) middle-magnification morphology; (F) middle-magnification morphology.

as seen in Figures 6A,C, the fusion zone extended up to $4 \times 0.03 \text{ mm} = 0.12 \text{ mm}$, spanning nearly the entire interfacial region. This extensive fusion can be attributed to the significant difference in melting points between steel and CuSn10. When the designed layer thickness is small, the metallographic observations reveal a mixed layer with diffuse boundaries, rather than the expected sharply defined multi-material interface. This occurs because the high thermal conductivity of CuSn10 promotes substantial heat transfer, causing partial remelting of previously deposited 316L layers and leading to nondirectional adhesion between the two materials.

With increasing gradient layer thickness, the interfacial transition between materials became more geometrically defined. However, such configurations also exhibited a greater propensity for forming micro defects, such as pores and cracks, at the interface. Micro cracks were observed within the fusion zones and along the boundaries of the 316L regions in all three samples, as marked by dashed circles in Figures 6A,B. No cracking was detected within the CuSn10 regions, which is consistent with the different thermophysical properties of the two materials.

At higher magnification (Figures 6D–F), dendritic cracks were seen to propagate from the fusion zone and the 316L boundary into the stainless steel matrix. This cracking behavior is attributed to the higher coefficient of thermal expansion of CuSn10 compared to steel, coupled with the strong interfacial adhesion. During cooling, the constrained shrinkage of CuSn10 induces tensile stresses that can initiate and extend cracks into the adjacent stainless steel.

Porosity formation in SLM processes is unavoidable, particularly in multi-material systems, where different material properties significantly influence porosity distribution. The results show that in sample 1 (Figure 6A, blue layer), porosity was concentrated in the 316L stainless steel region. In contrast, in samples 2 (Figure 6B) and 3 (Figure 6C), porosity was primarily found in the CuSn10 layers.

The pores in sample 1 and sample 2 are primarily distributed across different material layers, closely related to the initial materials used in their printed structures. In additive manufacturing of multi-material structures, the first layer of printed material determines the thermal history of the initial melt pool, substrate heat absorption capacity, and wetting behavior between the melt pool and substrate, significantly affecting the fusion quality of subsequent layers and

pore formation mechanisms. In sample 1, a 316L stainless steel initial layer was constructed. The low thermal conductivity and high melting point of 316L result in slow cooling rates and significant heat accumulation in the initial melt pool, leading to restricted gas escape in early layers and increased susceptibility to incomplete fusion pores or gas pores in the 316L region. The subsequently deposited CuSn10 layer, deposited on a sufficiently heated substrate, exhibited better melt pool stability, causing pores to concentrate mainly in the early 316L layer. Conversely, samples 2 and 3 used CuSn10 as the initial printing material. With its high thermal conductivity and low melting point, CuSn10 facilitates intense evaporation and rapid solidification of the initial melt pool, generating substantial vapor/gas that is rapidly captured by the “rapid solidification interface,” resulting in higher porosity in the CuSn10 region. The subsequently deposited 316L layer, deposited on a highly thermally conductive and preheated copper substrate, demonstrates more stable melt pools and uniform heat diffusion, leading to fewer pores in the 316L region.

3.2 Relationship between porosity and material layer thickness

To further examine the relationship between overall porosity and layer thickness, as well as the effect of porosity on thermal conductivity, systematic quantitative measurements were performed on cross-sectional regions of the samples. It should be noted that a single full cross-section provides only one metallographic view and may not sufficiently capture localized interfacial defects in gradient-structured materials. Therefore, instead of relying on a single cross-sectional area, this study employed a multi-section statistical strategy. Specifically, seven parallel metallographic sections were taken at equal intervals along the build direction within the interfacial region for each sample. This approach was designed to minimize the influence of incidental defects or local anomalies in any individual section and to enhance statistical robustness and repeatability through sampling across multiple planes.

The left panel of Figure 7 presents the measured actual thicknesses of the samples, while the right panel displays the corresponding number of layers deposited during powder spreading. For each selected cross-section, identical, randomly distributed rectangular regions were defined within a grid, and the average porosity within the yellow-framed areas was calculated to represent the overall material porosity. All micrographs were acquired at the same magnification. Image processing was performed using ImageJ software. Porosity was quantified by binarizing the images with an automatic local thresholding method and calculated as the ratio of the total pore area to the entire field area.

The measured results show that the overall porosity values for Samples 1, 2, and 3 are 12.814%, 15.421%, and 10.030%, respectively. Sample 3 exhibited the lowest porosity, indicating that its thinner-layer design was more effective in porosity control. The detailed porosity data are provided in Table 5. To further assess the consistency of porosity distribution, key statistical metrics are summarized in Table 5. Sample 1 showed the lowest standard deviation (1.519) and coefficient of variation (11.86%), reflecting the most uniform porosity distribution—likely a result of its balanced layer thickness, which minimized heat-induced defects. Sample

2 exhibited the highest variability (SD = 2.725, CV = 17.67%), indicating greater process fluctuations associated with thicker layers. Although Sample 3 achieved the lowest mean porosity, it demonstrated moderate dispersion (CV = 17.07%). Its highest normality value (0.45) supports the reliability of parametric analysis for this configuration.

Based on this framework, the influence of gradient layer-thickness design on porosity and its subsequent effect on thermal response were further investigated using the same multi-section sampling strategy. For each sample, seven representative regions were selected within the stainless steel zone, fusion zone, and CuSn10 zone, distributed from bottom to top along the build direction. As illustrated in Figure 8, a grid defines the overall sampling area, with red frames indicating the specific regions analyzed in each material zone. These regions were spaced equally and had identical dimensions to ensure representative coverage of the cross-section while minimizing the influence of local microstructural heterogeneity. This procedure follows standard metallographic sampling guidelines (ASTM E2109-15) and provides statistically reliable porosity data for subsequent analysis. Based on these data, statistical analyses were conducted to quantify the relationships between gradient layer thickness, porosity, and thermal response behavior.

Table 6 provides the detailed porosity data for Sample 1, while Table 7 summarizes the average porosity for single layers in Samples 2 and 3. The data analysis reveals that the porosity at the interface between the two phases is significantly higher than within single-phase layers, especially at the interface between CuSn10 and 316L stainless steel. This indicates that changes in process parameters (e.g., laser power) during Selective Laser Melting (SLM) fabrication may cause interface bonding to be mainly controlled by non-polar adhesion, which usually leads to higher porosity.

Based on the sampling positions, the build layers were categorized into three representative regions: the porous layer, the upper boundary, and the lower boundary. The porosity data corresponding to the porous layer are highlighted in bold within the tables. The porosity characteristics of each region were analyzed individually, and their variation trends are presented in Figure 9.

Figure 9 illustrates the porosity evolution across Samples 1–3. An overall increase in porosity with layer number is evident, indicating that porosity is influenced by the cumulative effects of layer thickness and thermal history during the build process.

For Sample 3, a distinct behavior is observed. When the layer number follows a descending layer thickness sequence, the porosity increases only slightly and remains nearly constant. In contrast, when the layer thickness increases with increasing layer number, the porosity rises progressively. This asymmetric response suggests that porosity in Sample 3 is more sensitive to increasing layer thickness than to decreasing layer thickness.

It should be noted that the study mainly focuses on the influence of the overall parameter macroscopic porosity (area percentage) on thermal performance. Although the microscopic morphology of pores (e.g., shape, size, connectivity) and its spatial distribution have important influences on the thermal conductivity and mechanical properties of materials, this variable is not analyzed in depth in order to focus on the dominant relationship between gradient layer thickness design, macroscopic porosity and thermal barrier

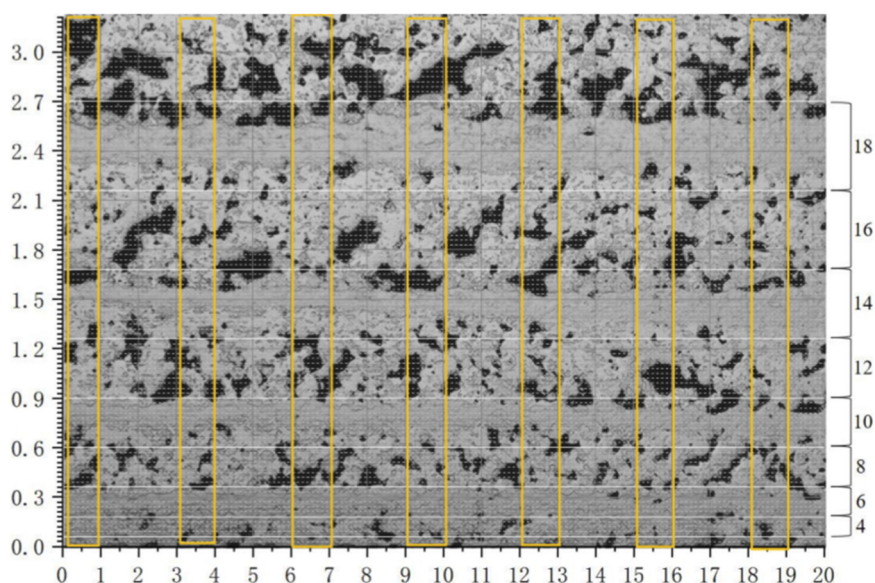


FIGURE 7
Selected area porosity map and quantitative measurement method.

properties. This part of the work can be further carried out in subsequent studies combined with advanced characterization methods such as CT microscopy and 3D reconstruction.

3.3 Thermal response

A COMSOL simulation analysis was performed disregarding porosity from the actual printing process. Initially, three configurations with progressively increasing interfacial densities—while maintaining identical compositional gradients and uniform material content—were designed for preliminary experimental validation. As illustrated in Figure 10A, the thermal barrier performance of the material enhanced with interfacial density.

Similarly, simulations of three linearly designed specimens (Section 2.3) yielded the results shown in Figure 10B. Specimens 1 and 2 exhibit comparable thermal barrier properties due to similar designs, while Specimen 3 attains performance equivalent to monolithic stainless steel owing to augmented interfaces, outperforming other specimens.

Thermal response measurements were conducted using thermocouples to simultaneously measure the top surface temperatures of three samples. 15 mm × 15 mm × 3.3 mm for thermocouple-based thermal response tests. Contact points were polished to Ra < 0.1 μm to ensure optimal thermal contact. Type K thermocouples (accuracy: ±0.5 °C) were bonded to sample surfaces using high-thermal-conductivity epoxy. A 100-μm layer of silicone-based thermal grease was applied between samples and the heating stage to eliminate interfacial air gaps. The samples were fixed on a constant-temperature heating stage, ensuring that the heat flow was perpendicular to the gradient-layered structures. The heating stage

was set to a temperature gradient from room temperature to 100 °C, and the temperature changes on the sample surfaces and substrates were recorded in real-time.

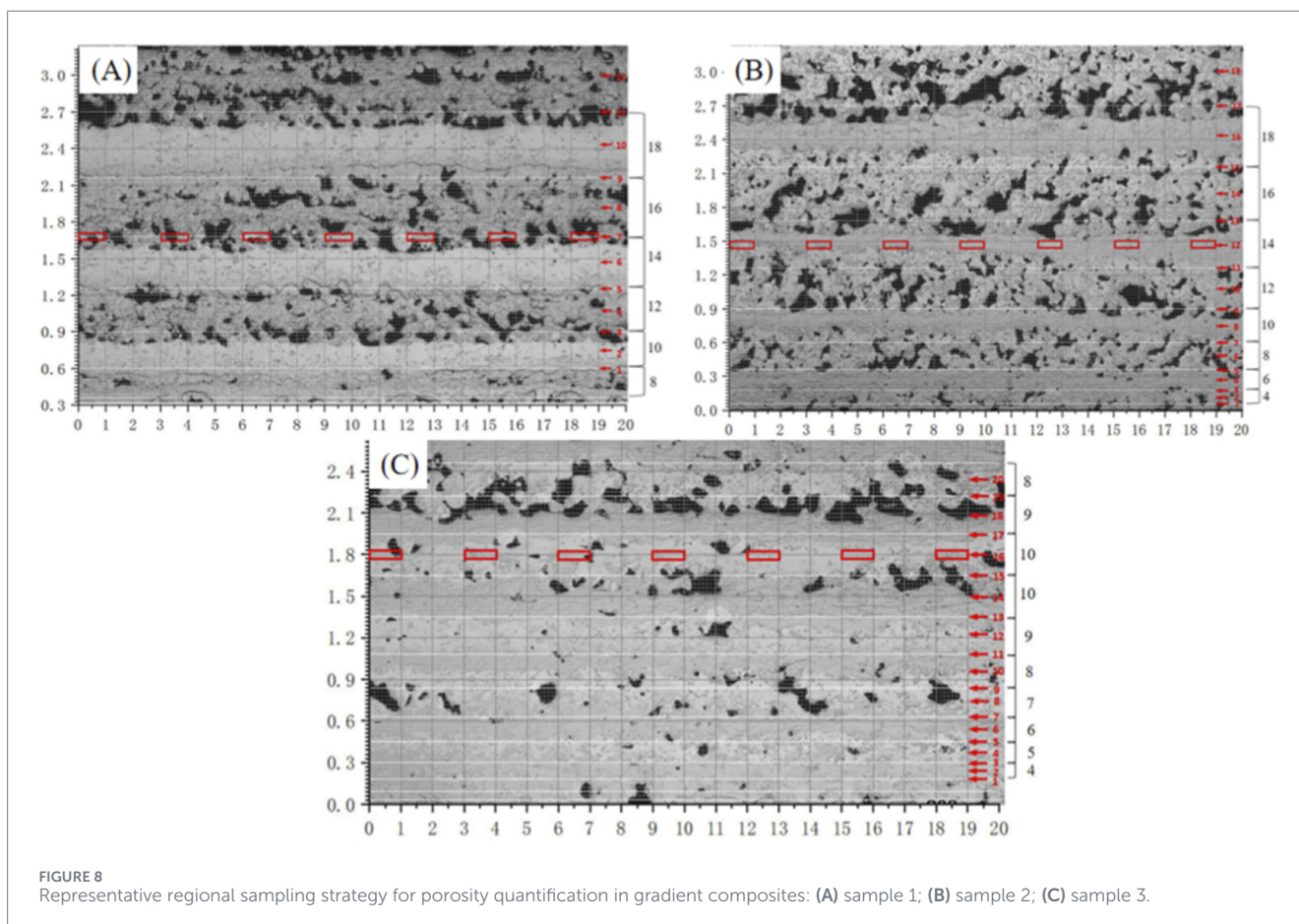
The temperature-time profiles in Figure 11 indicate comparable thermal response behavior between Samples 1 and 2 due to their analogous gradient structures. The marginally superior thermal conductivity of Sample 2 relative to Sample 1 is attributed to its elevated CuSn10 content. Sample 3 exhibited minimal porosity yet demonstrated significantly inferior thermal barrier performance compared to the other specimens, revealing a positive correlation between porosity and thermal barrier efficacy. Both functional layer configurations and porosity critically govern material thermal conductivity regulation. Gradient layer thickness design effectively modulated porosity distribution, thereby substantially enhancing thermal barrier properties.

Comparative analysis of experiments, simulations, and porosity quantification confirms that practical porosity effects surpass interfacial density impacts in simulations. Consequently, Sample 3 exhibited lower thermal barrier performance than Samples 1 and 2 despite higher interfacial density.

For transient hot-wire tests: Identical gradient designs scaled to 30 mm × 40 mm × 3.3 mm. Contact points were polished to Ra < 0.1 μm to ensure optimal thermal contact. Specimens were symmetrically positioned above/below the sensor. Measured thermal conductivities were 9.039 W/(m·K), 8.869 W/(m·K), and 12.237 W/(m·K)—all below monolithic stainless steel's 14 W/(m·K). This confirms significant thermal barrier enhancement through interfacial design, with Samples 1 and 2 demonstrating superior performance due to higher porosity in thick layers.

TABLE 5 Overall porosity obtained from region-based averaging of framed cross-sectional areas (%).

Sample ID	Meas. Area 1	Meas. Area 2	Meas. Area 3	Meas. Area 4	Meas. Area 5	Meas. Area 6	Meas. Area 7	Mean value	Standard deviation	Coefficient of variation	Normalized
Sample 1	11.187	15.648	13.324	11.991	13.420	11.455	12.674	12.814	1.519	11.86	0.25
Sample 2	20.299	14.314	14.575	15.745	17.117	14.293	11.606	15.421	2.725	17.67	0.15
Sample 3	9.583	8.078	9.509	9.906	8.523	11.721	12.887	10.030	1.712	17.07	0.45



4 Conclusion

This study systematically investigated the influence of gradient structure design—through linear variations in layer thickness—on the thermal response of CuSn10/316L composites fabricated by selective laser melting (SLM), with particular emphasis on the mediating role of porosity between structure and thermal properties. By integrating numerical simulations (assessing sensitivity to interfacial density and layer thickness) with experimental characterization (quantifying microstructure, porosity, and thermal performance), the following key conclusions were drawn.

4.1 Gradient layer thickness governs porosity formation

Layer thickness is a decisive factor controlling porosity distribution in SLM-processed gradient composites. Thinner gradient layers (e.g., Sample 3) promoted uniform energy transfer and melt-pool stability, facilitating gas escape and yielding lower porosity (averaging 10.03%). In contrast, thicker layers (e.g., Sample 1, 0.08 mm; Sample 2, 0.06 mm) induced localized heat accumulation, entrapping gases and raising porosity (up to 15.42% in Sample 2). This trend was consistent across both CuSn10 and

TABLE 6 Detailed porosity data of sample 1 (%).

Grade	Meas. Area 1	Meas. Area 2	Meas. Area 3	Meas. Area 4	Meas. Area 5	Meas. Area 6	Meas. Area 7	Mean value	
13	9.361	10.268	20.120	55.641	50.213	8.686	5.120	22.773	Upper boundary
12	7.879	8.081	1.01	62.424	81.01	63.232	34.343	36.854	Porous layer
11	91.852	27.407	7.963	29.63	15.741	5.741	62.593	34.418	Lower boundary
10	0	0	0	0	0	0	0	0	Copper layer
9	3.03	0	0	19.318	2.083	4.735	0.379	4.221	Upper boundary
8	1.903	0	34.884	27.484	20.507	0	0	12.111	Porous layer
7	36.553	37.879	17.045	0.947	2.273	24.432	28.977	21.158	Lower boundary
6	0	0	0	0	0	0	0	0	Copper layer
5	1.033	1.033	2.893	18.388	0.826	0.413	11.157	5.106	Upper boundary
4	12.810	4.339	0	0	29.339	6.818	0.62	7.704	Porous layer
3	23.678	31.116	24.298	33.554	22.531	28.26	18.182	25.946	Lower boundary
2	0	0	0	0	0	0	0	0	Copper layer
1	0	0	0	0.207	0	0.211	0	0.06	Upper boundary

Bold values indicate the average porosity of the porous layers and are used for plotting Figure 9.

TABLE 7 Average porosity of each gradient layer in samples 2 and 3 (%).

Grade	Sample 2	Sample 3	Grade	Sample 2	Sample 3
1	10.183	0.000	11	22.824	0.724
2	7.943	0.581	12	0.059	0.799
3	1.711	0.711	13	31.671	1.616
4	1.360	2.421	14	27.683	25.357
5	20.689	1.596	15	11.519	21.036
6	21.105	0.483	16	0.000	1.986
7	21.874	4.352	17	30.195	5.404
8	0.813	13.633	18	27.184	33.689
9	21.293	4.449	19	20.129	30.357
10	21.211	1.181	20	No data	19.727

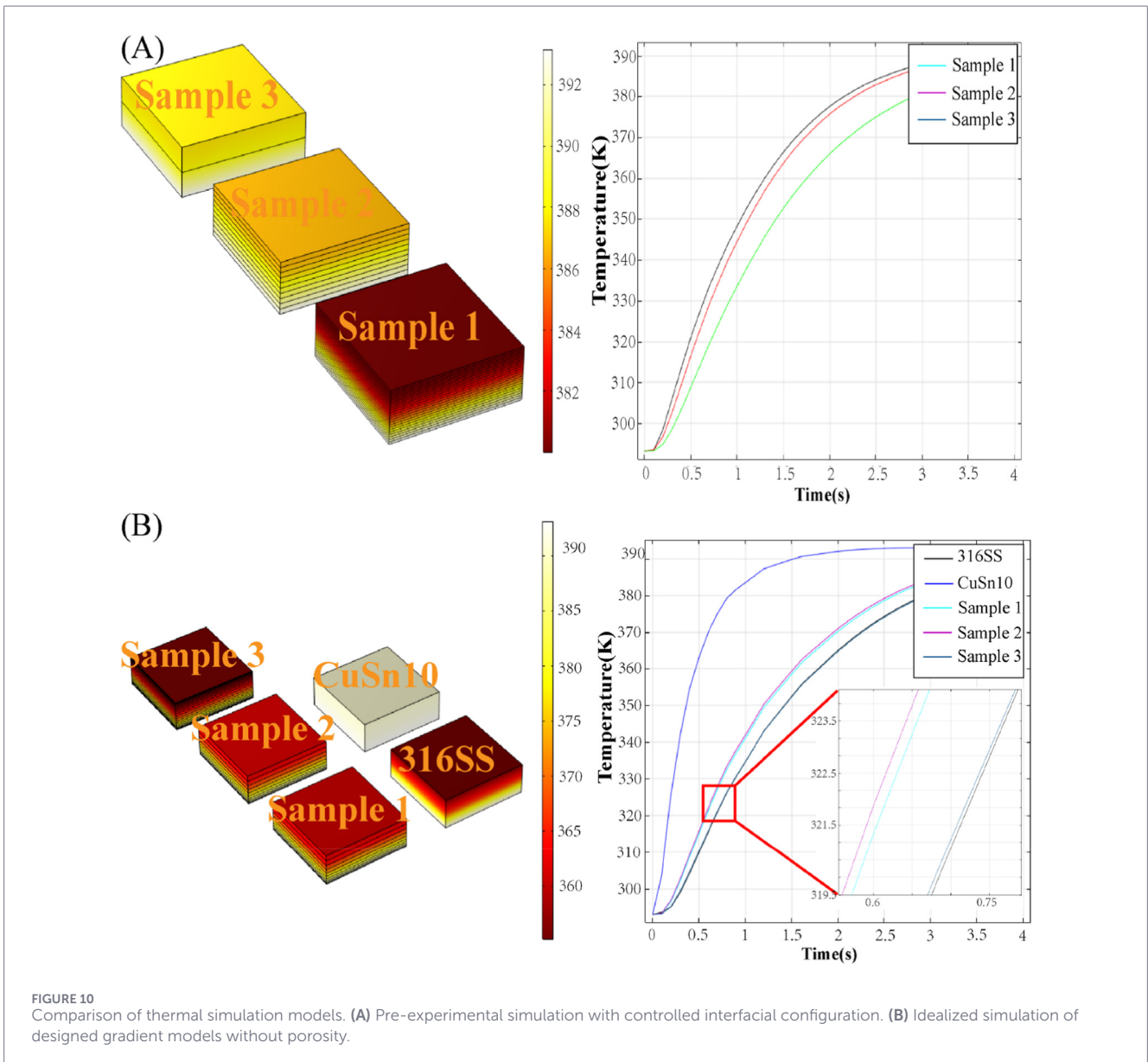
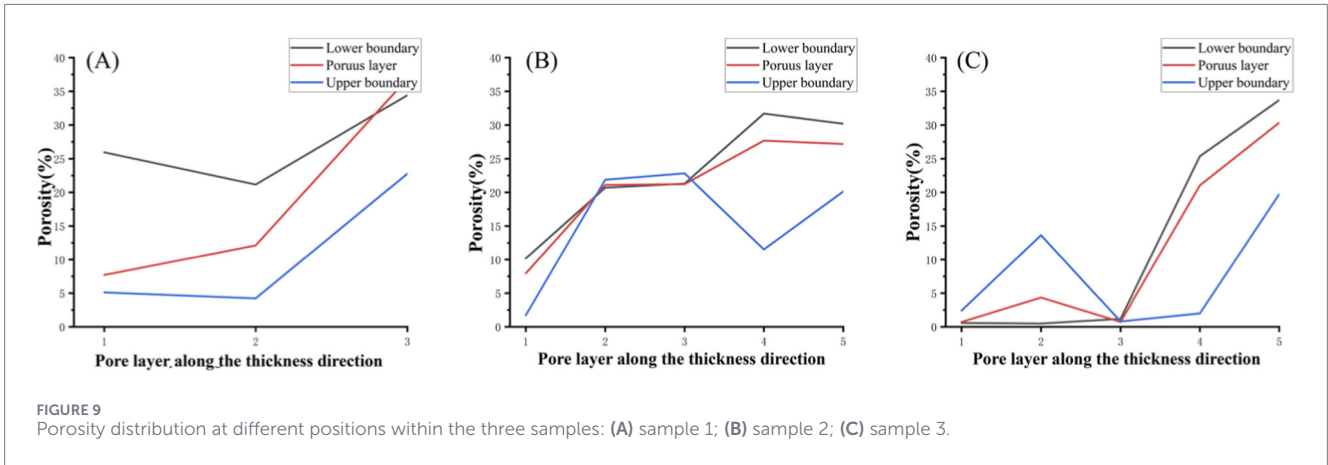
Bold values indicate porosity of the porous layers and are used for plotting Figure 9.

316L layers, underscoring the universal influence of layer thickness on melt-pool dynamics and defect generation.

4.2 Porosity drives thermal barrier performance

Simulations assuming pore-free interfaces predicted that increased interfacial layers would improve thermal barrier

performance by adding thermal resistance. Experimentally, however, porosity exerted a stronger influence: its thermal-resistance enhancement outweighed the effect of interface count. For instance, Sample 2—with the highest porosity (15.42%)—displayed the best thermal barrier performance, surpassing Sample 3 which had thinner layers and lower porosity (10.03%). This indicates that under the studied conditions, porosity-induced thermal resistance dominates barrier behavior,



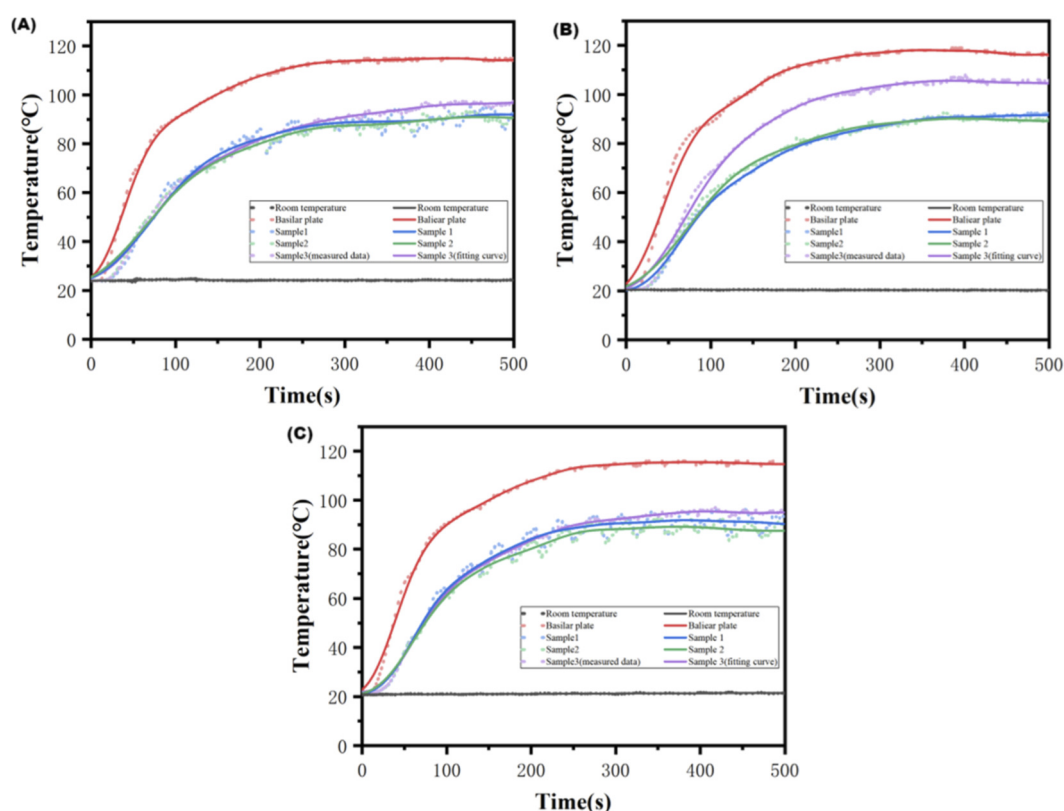


FIGURE 11
Curves of surface temperature over time measured three times: (A–C) are three experimental measurements, respectively.

surpassing the contribution from interfacial configuration alone.

Collectively, the results establish the mechanistic pathway “gradient layer thickness \rightarrow porosity evolution \rightarrow thermal barrier performance.” Optimization of gradient structures is inherently application-dependent due to competing requirements among thermal insulation, mechanical reliability, and structural weight. For CuSn10/316L systems, rational layer-thickness design should, while maintaining interfacial integrity, intentionally regulate porosity to enhance directional thermal resistance without inducing premature interfacial failure. The present findings provide both experimental evidence and a conceptual framework to support multi-objective design strategies for gradient composites in advanced thermal–structural applications.

Data availability statement

The original contributions presented in the study are included in the article/supplementary material, further inquiries can be directed to the corresponding author.

Author contributions

ZH: Conceptualization, Writing – original draft, Methodology, Data curation, Investigation. YW: Validation, Methodology,

Conceptualization, Writing – review and editing. SL: Methodology, Visualization, Investigation, Writing – review and editing. JH: Methodology, Writing – review and editing, Writing – original draft.

Funding

The author(s) declared that financial support was received for this work and/or its publication. The authors gratefully acknowledge Putian University and Jingdezhen Ceramic University, through the Program Research Grant 2024–2025: Fujian Central Government Guides Local Science and Technology Development Fund (Grant No. 2024L3016), Research Projects of Putian University (Grant No. 2024037), Startup Fund for Advanced Talents of Putian University (Grant No. 2024068 and Grant No. 2024141).

Conflict of interest

The author(s) declared that this work was conducted in the absence of any commercial or financial relationships that could be construed as a potential conflict of interest.

Generative AI statement

The author(s) declared that generative AI was used in the creation of this manuscript. Use AI for translation and polishing.

Any alternative text (alt text) provided alongside figures in this article has been generated by Frontiers with the support of artificial intelligence and reasonable efforts have been made to ensure accuracy, including review by the authors wherever possible. If you identify any issues, please contact us.

References

- AlMangour, B., Grzesiak, D., and Yang, J. M. (2017). Scanning strategies for texture and anisotropy tailoring during selective laser melting of TiC/316L stainless steel nanocomposites. *J. Alloys Compd.* 728, 424–435. doi:10.1016/j.jallcom.2017.08.022
- Attar, H., Ehtemam-Haghighi, S., Kent, D., and Dargusch, M. S. (2018). Recent developments and opportunities in additive manufacturing of titanium-based matrix composites: a review. *Int. J. Mach. Tools Manuf.* 133, 85–102. doi:10.1016/j.ijmactools.2018.06.003
- Balakrishnan, P., John, M. J., Pothen, L., Sreekala, M. S., and Thomas, S. (2016). “12 - Natural fibre and polymer matrix composites and their applications in aerospace engineering. *Adv. Comp. Material. Aerospace Eng. Process. Prop. Appl.* 365–383. doi:10.1016/B978-0-08-100037-3.00012-2
- Cadman, J. E., Zhou, S., Chen, Y., and Li, Q. (2013). On design of multi-functional microstructural materials. *J. Mater. Sci.* 48, 51–66. doi:10.1007/s10853-012-6643-4
- Cai, Z., Liu, B., Zou, X., and Cheng, H. M. (2018). Chemical vapor deposition growth and applications of two-dimensional materials and their heterostructures. *Chem. Reviews* 118 (13), 6091–6133. doi:10.1021/acs.chemrev.7b00536
- Choy, K. L. (2003). Chemical vapour deposition of coatings. *Prog. Materials Science* 48 (2), 57–170. doi:10.1016/s0079-6425(01)00009-3
- Dai, D., and Gu, D. (2014). Thermal behavior and densification mechanism during selective laser melting of copper matrix composites: simulation and experiments. *Mater. & Des.* 55, 482–491. doi:10.1016/j.matdes.2013.10.006
- Darabi, R., Azinpour, E., Reis, A., and de Sa, J. C. (2023). Multi-scale multi-physics phase-field coupled thermo-mechanical approach for modeling of powder bed fusion process. *Appl. Math. Model.* 122, 572–597. doi:10.1016/j.apm.2023.06.021
- Davis, L. C., and Artz, B. E. (1995). Thermal conductivity of metal-matrix composites. *J. Applied Physics* 77 (10), 4954–4960. doi:10.1063/1.359302
- Du Plessis, A., Yadroitsava, I., and Yadroitsev, I. (2020). Effects of defects on mechanical properties in metal additive manufacturing: a review focusing on X-ray tomography insights. *Mater. & Des.* 187, 108385. doi:10.1016/j.matdes.2019.108385
- El-Galy, I. M., Ahmed, M. H., and Bassiouny, B. I. (2017). Characterization of functionally graded Al-SiCp metal matrix composites manufactured by centrifugal casting. *Alexandria Eng. J.* 56 (4), 371–381. doi:10.1016/j.aej.2017.03.009
- Ferreira, A. D. B. L., Nóvoa, P. R. O., and Marques, A. T. (2016). Multifunctional material Systems: a state-of-the-art review. *Compos. Struct.* 151, 3–35. doi:10.1016/j.compstruct.2016.01.028
- Guo, S., Li, Y., Gu, J., Liu, J., Peng, Y., Wang, P., et al. (2023). Microstructure and mechanical properties of Ti6Al4V/B4C titanium matrix composite fabricated by selective laser melting (SLM). *J. Mater. Res. Technol.* 23, 1934–1946. doi:10.1016/j.jmrt.2023.01.126
- Hasanov, S., Alkunte, S., Rajeshirke, M., Gupta, A., Huseynov, O., Fidan, I., et al. (2021). Review on additive manufacturing of multi-material parts: progress and challenges. *J. Manuf. Mater. Process.* 6 (1), 4. doi:10.3390/jmmp6010004
- Ishitani, T., and Yaguchi, T. (1996). Cross-sectional sample preparation by focused ion beam: a review of ion-sample interaction. *Microsc. Research Technique* 35 (4), 320–333. doi:10.1002/(SICI)1097-0029(19961101)35:4<320::AID-JEMT3>3.0.CO;2-Q
- Li, N., Liu, W., Wang, Y., Zhao, Z., Yan, T., Zhang, G., et al. (2021). Laser additive manufacturing on metal matrix composites: a review. *Chin. J. Mech. Eng.* 34, 1–16. doi:10.1186/s10033-021-00554-7
- Liu, Y. B., Lim, S. C., Lu, L., and Lai, M. O. (1994). Recent development in the fabrication of metal matrix-particulate composites using powder metallurgy techniques. *J. Mater. Sci.* 29, 1999–2007. doi:10.1007/bf01154673
- Liu, Z., Zhao, D., Wang, P., Yan, M., Yang, C., Chen, Z., et al. (2022). Additive manufacturing of metals: microstructure evolution and multistage control. *J. Mater. Sci. & Technol.* 100, 224–236. doi:10.1016/j.jmst.2021.06.011
- Mao, X., Liu, S., Tan, J., Hu, H., Lu, C., and Xuan, D. (2023). Multi-objective optimization of gradient porosity of gas diffusion layer and operation parameters in PEMFC based on recombination optimization compromise strategy. *Int. J. Hydrogen Energy* 48 (35), 13294–13307. doi:10.1016/j.ijhydene.2022.12.226

Publisher's note

All claims expressed in this article are solely those of the authors and do not necessarily represent those of their affiliated organizations, or those of the publisher, the editors and the reviewers. Any product that may be evaluated in this article, or claim that may be made by its manufacturer, is not guaranteed or endorsed by the publisher.

- Marattukalam, J. J., Karlsson, D., Pacheco, V., Beran, P., Wiklund, U., Jansson, U., et al. (2020). The effect of laser scanning strategies on texture, mechanical properties, and site-specific grain orientation in selective laser melted 316L SS. *Mater. & Des.* 193, 108852. doi:10.1016/j.matdes.2020.108852
- Markandan, K., Lim, R., Kanaujia, P. K., Seetoh, I., bin Mohd Rosdi, M. R., Tey, Z. H., et al. (2020). Additive manufacturing of composite materials and functionally graded structures using selective heat melting technique. *J. Mater. Sci. & Technol.* 47, 243–252. doi:10.1016/j.jmst.2019.12.016
- Markworth, A. J., Ramesh, K. S., and Parks, W. P. (1995). Modelling studies applied to functionally graded materials. *J. Mater. Sci.* 30, 2183–2193. doi:10.1007/bf01184560
- Najmon, J. C., Raeisi, S., and Tovar, A. (2019). Review of additive manufacturing technologies and applications in the aerospace industry. *Addit. Manufacturing Aerospace Industry*, 7–31. doi:10.1016/B978-0-12-814062-8.00002-9
- Narayana, K. J., and Burela, R. G. (2018). A review of recent research on multifunctional composite materials and structures with their applications. *Mater. Today Proc.* 5 (2), 5580–5590. doi:10.1016/j.matpr.2017.12.149
- Pandey, V., Seetharam, R., and Chelladurai, H. (2024). A comprehensive review: discussed the effect of high-entropy alloys as reinforcement on metal matrix composite properties, fabrication techniques, and applications. *J. Alloys Compd.* 1002, 175095. doi:10.1016/j.jallcom.2024.175095
- Pang, X., Song, Y., Shi, N., Xu, M., Zhou, C., and Chen, J. (2022). Design of zero thermal expansion and high thermal conductivity in machinable xLFCs/Cu metal matrix composites. *Compos. Part B Eng.* 238, 109883. doi:10.1016/j.compositesb.2022.109883
- Raghavendra, S., Jayashree, P., Rita, D. A., Piras, G., Scheider, D., Chemello, M., et al. (2023). Wear and material characterization of CuSn10 additively manufactured using directed energy deposition. *Addit. Manuf. Lett.* 6, 100136. doi:10.1016/j.addlet.2023.100136
- Sathish, M., Radhika, N., and Saleh, B. (2021). A critical review on functionally graded coatings: methods, properties, and challenges. *Compos. Part B Eng.* 225, 109278. doi:10.1016/j.compositesb.2021.109278
- Shi, J., and Wang, Y. (2020). Development of metal matrix composites by laser-assisted additive manufacturing technologies: a review. *J. Mater. Sci.* 55 (23), 9883–9917. doi:10.1007/s10853-020-04730-3
- Sidhu, S. S., Kumar, S., and Batish, A. (2016). Metal matrix composites for thermal management: a review. *Crit. Rev. Solid State Mater. Sci.* 41 (2), 132–157. doi:10.1080/10408436.2015.1076717
- Tan, C., Chew, Y., Bi, G., Wang, D., Ma, W., Yang, Y., et al. (2021). Additive manufacturing of steel-copper functionally graded material with ultrahigh bonding strength. *J. Mater. Sci. & Technol.* 72, 217–222. doi:10.1016/j.jmst.2020.07.044
- Thomas, J. P., and Qidwai, M. A. (2004). Mechanical design and performance of composite multifunctional materials. *Acta Mater.* 52 (8), 2155–2164. doi:10.1016/j.actamat.2004.01.007
- Tofail, S. A. M., Koumoulos, E. P., Bandyopadhyay, A., Bose, S., O'Donoghue, L., and Charitidis, C. (2018). Additive manufacturing: scientific and technological challenges, market uptake and opportunities. *Mater. Today* 21 (1), 22–37. doi:10.1016/j.mattod.2017.07.001
- Tonyali, B., Sun, H., Liu, Z. K., Keist, J., and Beese, A. M. (2024a). Tailoring the coefficient of thermal expansion in a functionally graded material: Al alloyed with Ti-6Al-4V using additive manufacturing. *J. Alloys Compd.* 1009, 176971. doi:10.1016/j.jallcom.2024.176971
- Tonyali, B., Sun, H., Bocklund, B., Borgonia, J. P., Otis, R. A., Shang, S. L., et al. (2024b). Additively manufactured Ni-20Cr to V functionally graded material: computational predictions and experimental verification of phase formations. *J. Alloys Compd.* 985, 174011. doi:10.1016/j.jallcom.2024.174011
- Ullah, A., Ur Rehman, A., Salamci, M. U., Ptiir, F., and Liu, T. (2022). The influence of laser power and scanning speed on the microstructure and surface morphology of Cu2O parts in SLM. *Rapid Prototyp. J.* 28 (9), 1796–1807. doi:10.1108/rtpj-12-2021-0342

- Yan, C., Li, S., Yang, L., and He, L. (2019). Investigation of FEF process liquid phase migration using orthogonal design of experiments. *Rapid Prototyp. J.* 25 (2), 388–396. doi:10.1108/rpj-10-2016-0173
- Yang, X., Wei, P., Wang, X., and He, Y. L. (2020). Gradient design of pore parameters on the melting process in a thermal energy storage unit filled with open-cell metal foam. *Appl. Energy* 268, 115019. doi:10.1016/j.apenergy.2020.115019
- Yap, C. Y., Chua, C. K., Dong, Z. L., Liu, Z. H., Zhang, D. Q., Loh, L. E., et al. (2015). Review of selective laser melting: materials and applications. *Appl. Physics Reviews* 2 (4), 041101. doi:10.1063/1.4935926
- Yen, H. J., and Liou, G. S. (2019). Design and preparation of triphenylamine-based polymeric materials towards emergent optoelectronic applications. *Prog. Polym. Sci.* 89, 250–287. doi:10.1016/j.progpolymsci.2018.12.001
- Yuan, X., Chen, M., Yao, Y., Guo, X., Huang, Y., Peng, Z., et al. (2021). Recent progress in the design and fabrication of multifunctional structures based on metamaterials. *Curr. Opin. Solid State Mater. Sci.* 25 (1), 100883. doi:10.1016/j.cossms.2020.100883
- Zhang, C., Chen, F., Huang, Z., Jia, M., Chen, G., Ye, Y., et al. (2019). Additive manufacturing of functionally graded materials: a review. *Mater. Sci. Eng. A* 764, 138209. doi:10.1016/j.msea.2019.138209